EES Solar

PAPER

View Article Online
View Journal | View Issue

Cite this: *EES Sol.*, 2026, **2**, 149

The role of terminal functional groups in molecular passivation of the perovskite/hole-selective layer interface

Mahboubeh Hadadian, *[a] Thomas W. Gries, [b] G. Krishnamurthy Grandhi, [c] Emil Rosqvist, [d] Rustem Nizamov, [a] Sari Granroth, [e] Paola Vivo, [c] Ronald Österbacka, [f] Jan-Henrik Smått, [d] Antonio Abate [b] and Kati Miettunen [a]

The objective of this study is to investigate how terminal functional groups in passivating agents influence the optoelectronic properties and photovoltaic performance of perovskite solar cells. Engineering the perovskite/hole-selective layer interface is critical for effective defect passivation, reduced interfacial recombination, improved charge extraction, optimized energy level alignment, and overall enhancement of device performance. While various molecular strategies have been proposed, the role of specific functional groups in passivating interfacial defects remains poorly understood. Here, a comparative investigation is conducted on three molecules with identical five-carbon backbones but distinct functionalities ammonium (*n*-pentylammonium iodide), carboxylic acid (valeric acid), and a bifunctional ammonium–carboxylic acid (5-ammonium valeric acid iodide) as passivating agents in perovskite/hole-selective layer interface. Optoelectronic characterization studies including photoluminescence, surface photovoltage, and conductive atomic force microscopy reveal distinct functional group-dependent variations in trap passivation, carrier dynamics, and interfacial conductivity. Devices based on surface-treated perovskites with single-functional group agents exhibit improved open-circuit voltage (V_{OC}) and fill factor (FF), confirming efficient trap suppression and charge extraction. In contrast, the bifunctional molecule, despite effective trap passivation, limits the hole extraction. This work highlights the critical role of molecular functionality in determining interfacial interactions and charge transfer, offering a strategic pathway for interface engineering in perovskite photovoltaics.

Received 23rd September 2025
Accepted 9th October 2025

DOI: 10.1039/d5el00156k

rsc.li/EESSolar

Broader context

The rapid efficiency gains of perovskite solar cells (PSCs) have propelled them to the forefront of photovoltaic technologies. Yet, interfacial defects, particularly at the perovskite/hole-selective layer (HSL) interface, remain a key bottleneck, limiting charge extraction and contributing to low efficiency and instability. While molecular passivation has emerged as a promising strategy to address these challenges, the specific role of terminal functional groups in modifying the interfacial energetics and defect interactions is a critical aspect and receives growing attention in interface engineering. In this work, we investigate three structurally related molecules bearing ammonium, carboxylic acid, and bifunctional ammonium–carboxyl terminals to isolate functional group effects on the perovskite/HSL interface. Through in-depth optoelectronic characterization and surface photovoltage spectroscopy, we uncover distinct structure–function relationships that influence interlayer formation, trap passivation, and charge extraction. This study quantifies charge extraction dynamics at this interface using surface photovoltage. The insights presented here offer a rational basis for designing molecular passivators, with implications for advancing the efficiency of PSCs.

[a]*Department of Mechanical and Materials Engineering, Faculty of Technology, University of Turku, Vesilinnantie 5, Turku 20500, Finland. E-mail: mahboubeh.hadadian@utu.fi*

[b]*Helmholtz-Zentrum Berlin für Materialien und Energie (HZB), 14109, Berlin, Germany*

[c]*Hybrid Solar Cells, Faculty of Engineering and Natural Sciences, Tampere University, P.O. Box 541, Tampere FI-33720, Finland*

[d]*Laboratory of Molecular Science and Engineering, Henriksgatan 2, Åbo Akademi, Turku 20500, Finland*

[e]*Department of Physics and Astronomy, University of Turku, Turku 20014, Finland*

[f]*Physics and Center for Functional Materials, Faculty of Science and Engineering, Åbo Akademi University, Henriksgatan 2, Turku 20500, Finland*

1. Introduction

While perovskite solar cells (PSCs) have demonstrated remarkable progress in power conversion efficiencies (PCEs), surpassing 27% in single-junction devices,[1] further performance gains and operational stability rely on effective defect passivation at critical interfaces. In particular, the chemical mechanisms by which functional groups in molecular passivation agents influence interfacial defect passivation, interlayer formation, and charge transport remain poorly understood. In

this work, we systematically investigate the role of terminal functional groups in interfacial passivation by employing organic cations with identical alkyl chain lengths but differing functionalities.

The emergence of PSCs as a leading photovoltaic technology originates from their exceptional optoelectronic properties, including high absorption coefficients, tunable band gaps, low exciton binding energies, and long carrier diffusion lengths.[2,3] Combined with low-temperature solution-processable fabrication, these characteristics have enabled their rapid development and their integration into tandem configurations with silicon to reduce the levelized cost of electricity. The prototypical 3D perovskite structure (ABX_3) comprises an organic or inorganic A-site cation (*e.g.*, FA^+, MA^+, and Cs^+), Pb^{2+} at the B-site, and a halide X-site anion (Cl^-, Br^-, and I^-). However, film polycrystallinity leads to undercoordinated Pb^{2+} ions, metallic Pb (Pb^0) defects, and charged defect sites at grain boundaries and surfaces, forming non-radiative recombination centers detrimental to the open-circuit voltage (V_{OC}) and the fill factor (FF).[4,5] Furthermore, device degradation is accelerated by intrinsic factors such as ion migration and defects. Interfacial defects, particularly at the perovskite/hole-selective layer (HSL) interface, are a dominant loss channel, with trap densities up to five orders of magnitude higher than those in the bulk.[6] Molecular passivation strategies have been widely explored to suppress interfacial recombination and improve device performance, leveraging the versatility of organic compounds in functional group tuning and solution processability.[7]

Following early reports on fullerene-based passivation,[8] a broad range of materials, including polymers,[9] graphene,[10] Lewis acids/bases,[11] and 2D perovskites,[12,13] have been employed to mitigate interfacial defects. Bulky organic cations are particularly promising, forming quasi-2D Ruddlesden–Popper (RP) phases [$(RNH_3)_2A_{n-1}Pb_nX_{3n+1}$] that act as 2D capping layers, enhancing both PCE and stability (n is the number of octahedra in the 2D layer and R is the longer chained organic cation).[14] Functional groups such as fluorine, ammonium, carboxylic acid, and zwitterionic moieties enable surface interaction *via* electrostatic attraction or coordination bonding.[15,16] Notably, the electronic character of these functional groups plays a key role in passivation efficacy. For example, Zhuang *et al.*[17] showed that phenethylammonium iodide derivatives with electron-donating groups (*e.g.*, methoxy and methyl) outperformed those with electron-withdrawing groups (*e.g.*, nitro) in suppressing interfacial recombination due to stronger electrostatic interaction between the benzene ring and the undercoordinated Pb^{2+} ions. Similarly, carboxyl-containing molecules have demonstrated effective surface passivation through hydrogen bonding or Lewis acid–base interactions.[18]

While individual passivation agents, featuring functional groups such as ammonium,[19,20] thiol,[21] and phosphonic acid,[22–24] have been studied, comparative analysis remains limited and thus insight into the role of the terminal group is lacking.[13] Comparative studies that can isolate the role of terminal functionality are essential for developing a rational framework to design passivation agents that balance strong surface coordination with favorable interfacial energetics, enabling more efficient and stable PSCs. In particular, controlled comparisons that eliminate variations in molecular backbone length, rigidity, and steric hindrance, while evaluating mono-, bi-, or multifunctional molecules, are critical to uncovering structure–function relationships in passivation. Our study employs a structurally controlled molecular platform consisting of organic cations with identical five-carbon alkyl backbones but varied terminal groups ($–NH_3^+$, –COOH, and bifunctional). This approach enables a direct comparison of terminal group effects on defect passivation, charge separation, and quasi-2D RP phase formation. By including both mono- and bifunctional molecules, we reveal mechanistic differences in how terminal groups interact with the perovskite surface and influence charge transport, recombination, and surface properties.

Moreover, a comprehensive understanding of how functional group chemistry dictates interfacial structure–property relationships is still lacking. By addressing this gap, our work informs the design of molecular passivation agents to enhance PSC performance through precise interfacial engineering. We uniquely isolate the effect of functionality of specific groups such as ammonium and carboxyl groups from structural factors, including chain length and steric bulk (aliphatic and aromatic nature). Valeric acid (VA) or pentanoic acid, containing a carboxylic group, *n*-pentylammonium iodide (*n*-PentI), with an ammonium group, and 5-ammonium valeric acid iodide (5-AVAI) with both functional groups are selected to investigate the role of these functionalities in passivating the perovskite/HSL interface. These molecules, though structurally straightforward, offer distinct functional groups and could enable new insights into passivation chemistry at the perovskite/HSL interface. Moreover, the use of *n*-PentI and VA as passivating agents at the interface has remained unexplored so far. By combining conductive atomic force microscopy (C-AFM), time-resolved photoluminescence (trPL) and transient surface photovoltage (trSPV) measurements, we probe how terminal functionality influences charge carrier dynamics and interfacial passivation, providing mechanistic insight into mono *versus* bifunctional passivators. Through a detailed study of the perovskite/HSL interface, we find a strong correlation between the nature of the functional group, the formation of quasi-2D RP interlayers, and photovoltaic performance metrics such as V_{OC} and FF. Our findings highlight the superior performance of ammonium-functionalized molecules, which promotes the selective formation of $n = 2$ RP phases and enables efficient surface passivation and charge extraction. This study provides critical insight into the rational design principles of passivation molecules for achieving high-efficiency PSCs.

2. Results and discussion

Surface defects on the perovskite surface have been studied both experimentally and theoretically and it has been reported that positively/negatively charged defects on the perovskite surface and grain boundaries unfavorably affect the performance of PSCs.[25–27] These species create energy levels within the

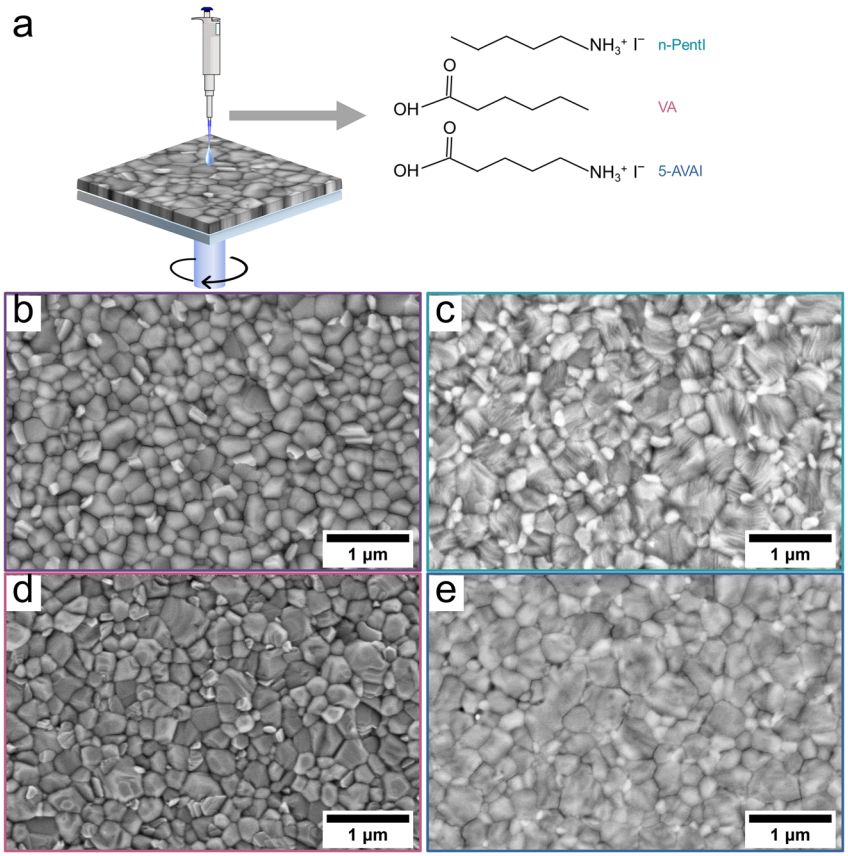

Fig. 1 Interface layer deposition and morphological effects. (a) Schematic of deposition of the interface layer and the molecular structures of the cations and molecule. SEM images of (b) pristine CsFAMA film, (c) *n*-PentI, (d) VA, and (e) 5-AVAI surface-treated perovskite films.

forbidden gap, acting as trap states for charge carriers. Incorporating passivation layers at the perovskite surface is an effective strategy in passivating the traps and enhancing the performance and lifetime of the devices. The chemical structures of passivation agents used in this study, VA, *n*-PentI, and 5-AVAI, are shown in Fig. 1a.

A widely used triple cation, double halide perovskite, $Cs_{0.05}(FA_{0.83}MA_{0.17})_{0.95}Pb(I_{0.83}Br_{0.17})_3$, CsFAMA, is employed as a benchmark due to its popularity in the perovskite literature. The perovskite layer was fabricated using a one-step antisolvent-assisted spin-coating process, producing a compact and pinhole free layer. The passivation layers were deposited on top of the annealed perovskite film. Passivation molecules may also penetrate through the grain boundaries of polycrystalline films. As shown in Fig. 1a, to ensure non-destructive deposition, the passivation layer was applied dynamically using a solvent mixture of chlorobenzene (CB) and isopropanol (IPA). In contrast, static spin-coating deposition, particularly with IPA solvent, is detrimental for the perovskite layer, resulting in uneven film formation, poor crystallinity, and lower optical absorption, all of which can compromise device performance. Fig. S1 shows the ultraviolet-visible (UV-Vis) absorption spectra of the perovskite layers fabricated using static deposition with varying durations of IPA exposure.

2.1. Morphological and structural characterization

A comparison of the microstructure of the treated and untreated perovskite films is shown in Fig. 1b–e. The top view scanning electron microscope (SEM) image of the reference pristine perovskite (Fig. 1b) shows compact and pinhole-free morphology with well-defined grain boundaries and a relatively smooth surface. An overall increase in grain size after the treatment with passivation agent process is observed for the samples, especially with *n*-PentI and 5-AVAI passivation layers, confirming the surface reconstruction of the perovskite surface. The morphology in the SEM image of the perovskite film treated with *n*-PentI solution (Fig. 1c) indicates the growth of a 2D RP perovskite phase, which can effectively passivate the surface defects. Less prominent grain boundaries in the *n*-PentI treated samples can be correlated with the formation of the RP overlayer modifying the interfacial properties of the film.[28] The VA treated sample (Fig. 1d) retains a morphology similar to that of the pristine sample since this surface passivator lacks an ammonium functional group to contribute to the formation of a low-dimensional perovskite overlayer. The surface of the sample treated with 5-AVAI (Fig. 1e) displays the formation of an insulating overlayer on top of the perovskite grains, which could be attributed to the formation of a 2D perovskite and an organic insulating phase. Such layers may introduce barriers to charge

transport, which could negatively impact the FF and overall PCE of solar cells.

The surface chemical composition (within 10 nm) of the samples, including pristine perovskite and surface-treated perovskite films with *n*-PentI, VA, and 5-AVAI was determined using X-ray photoelectron spectroscopy (XPS). The binding energies were calibrated to the C 1s peak of adventitious carbon (C–C), set at 284.8 eV. Fig. 2a shows the Pb 4f spectra of the samples, with characteristic peaks observed at binding energies (E_B) of 143 eV and 138 eV, corresponding to the Pb $4f_{5/2}$ and Pb $4f_{7/2}$ features, respectively. The Pb $4f_{7/2}$ and Pb $4f_{5/2}$ core levels were deconvoluted into two components,[29] representing

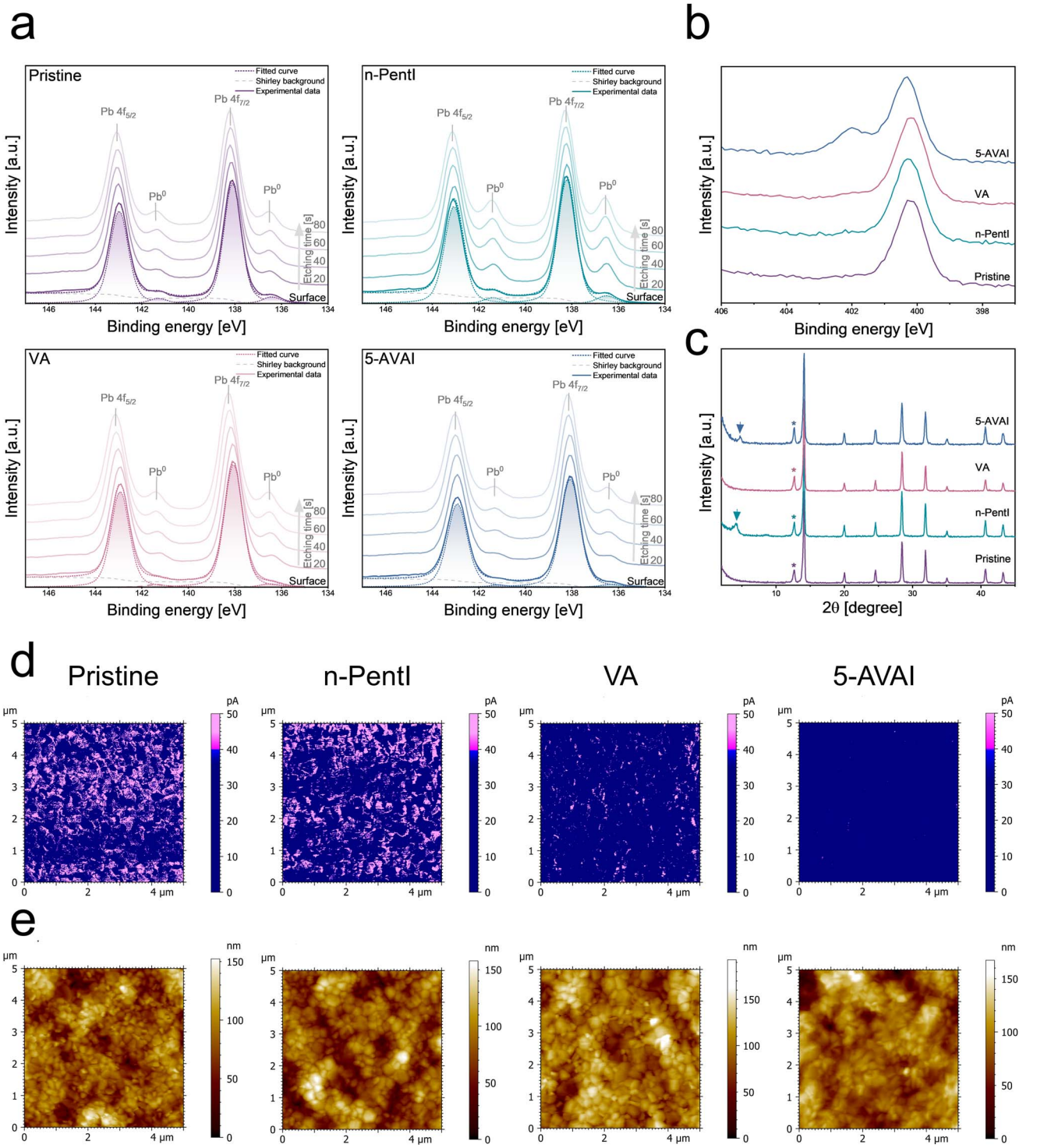

Fig. 2 Structural, compositional, and morphological characterization. XPS elemental scans of (a) Pb 4f and (b) N 1s. (c) XRD patterns of pristine and surface-modified perovskite thin films (PbI_2 peaks at $2\theta = 12.5°$ are marked by asterisks). (d) C-AFM images of the perovskite films. (e) Representative AFM images showcasing the topography of the perovskite films at 5 μm × 5 μm.

distinct chemical states, metallic Pb (Pb^0) and Pb^{2+} associated with the perovskite lattice. For Pb $4f_{7/2}$, Pb^0 and Pb^{2+} peaks appeared at 136.5 eV and 138.1 eV, respectively, consistent with previously reported values.[30] The surface Pb^0/Pb^{2+} intensity ratios were 0.05, 0.06, 0.02, and 0.02 for the pristine, *n*-PentI, VA, and 5-AVAI perovskite films, respectively. The lower ratios in VA- and 5-AVAI-treated samples indicate the effective interaction of the carboxylic acid group with metallic lead, likely suppressing Pb^0 formation. The possible impact of X-ray exposure on the Pb 4f spectra was evaluated by collecting snapshot spectra before and after collecting the high-resolution scans. The snapshot spectra collected remained consistent, indicating that X-ray exposure had minimal impact on the Pb 4f signal.

Depth profiling was performed using low-energy Ar cluster sputtering to estimate the Pb^0/Pb^{2+} ratio in the near-surface region while minimizing Pb^0 generation from ion damage. The depth profile shows that the Pb^0/Pb^{2+} ratio increases upon etching. After 80 seconds of sputtering, the Pb^0/Pb^{2+} ratio increases relative to the surface values. It is worth noting that samples were stored in a high vacuum (X-rays and flood gun off) for several hours, after which changes in surface composition were reassessed. The Pb^0 signal increased slightly across all samples, suggesting vacuum-induced surface reconstruction. Table S1 shows the Pb^0/Pb^{2+} intensity ratios. Further insights are provided by N 1s spectra (Fig. 2b). The pristine perovskite film displays a single peak at 400.2 eV, attributed to the NH_2 group of the FA^+ cation, the dominant cation in FAMACs triple-cation perovskite. Upon treatment with 5-AVAI, an additional feature emerges, corresponding to the R–NH_3^+ moiety of 5-AVA.

Fig. 2c presents the X-ray diffraction (XRD) patterns of the pristine and surface-treated perovskite films. All four films show characteristic XRD patterns associated with the 3D CsFAMA perovskite phase.[31] In addition, the peak at ~12.6° 2θ indicates that all samples contain PbI_2. The XRD patterns of the surface-treated perovskite films are similar to those of the pristine film showing a well-preserved crystallinity in the perovskite stacking layer. The VA-treated perovskite film maintains an identical diffraction pattern to the pristine sample with the same crystal structure, while new diffraction peaks at 4.2° and 4.8° 2θ appear in the XRD patterns of *n*-PentI and 5-AVAI treated films. XRD peaks at 10° 2θ are considered a sign for 2D perovskite species with the formula of R_2PbI_4, showing the surface reconstruction and *in situ* growth of a 2D RP perovskite phase.[32] However, these peaks differ from those of the pure 2D perovskites, *n*-$Pent_2PbI_4$ and 5-AVA_2PbI_4. Literature reports indicate that pure 2D perovskites with $n = 2$, such as *n*-$PentI_2A_3PbX_7$, exhibit diffraction peaks in a similar 2θ range.[33] To investigate the origin of these peaks further, we synthesized 2D perovskite layers with $n = 1$ of the octahedron layers by mixing *n*-PentI and PbI_2 or 5-AVAI and PbI_2 in a 2 : 1 stoichiometric ratio. The XRD patterns of these reference 2D perovskites (Fig. S2) feature distinct peaks at 6.02° and 7.7° 2θ for *n*-$PentI_2PbI_4$ and 5-AVA_2PbI_4, respectively. Therefore, the 2D layer has a structure of $n = 2$ on top of the perovskite layer. Additionally, a diffraction peak at around 4° 2θ was previously reported for 5-AVAI-based passivation layers, supporting the hypothesis that the passivation layer differs from a pure 2D 5-AVA_2PbI_4 phase and instead corresponds to an $n = 2$ structure.[34]

C-AFM was employed to investigate the spatial variations in surface conductivity across the surface of perovskite films, revealing the impact of passivation layers on conductivity (Fig. S3). The presence of passivation layers led to smaller conductive regions (applying a bias of 0.2 V over the sample and using a measured current of 40 pA as cutoff), seen as magenta in Fig. 2d. The C-AFM images highlight significant variations in conductivity at the nanoscale, with the perovskite film treated with 5-AVAI exhibiting the lowest, and a negligible surface conductivity among the samples (smallest area, approx. 0.01%). This reduction in conductivity confirms the presence of insulating cations introduced by the passivation agents. Conductivity of 2D perovskites is typically low due to their anisotropic structure, where bulky organic cations act as insulating layers between inorganic sheets.[35] In contrast, the conductivity of the perovskite film treated with *n*-PentI remained largely unchanged (approx. 20.6%). VA treated films also showed a decrease in surface conductivity (approx. 4.3%), compared to the pristine perovskite film (approx. 22.6%). The C-AFM measurements further revealed that the 5-AVAI-treated sample exhibited fewer high-conductivity regions, supporting the hypothesis of this passivation agent reducing charge transport at the surface.

The corresponding AFM images (Fig. 2e) and roughness parameters (Table S2) reveal that passivated samples show increased height variations, reflected in higher S_a (arithmetical mean height) and S_q (root mean square height). S_q is approx. 21 nm for the pristine surface and 25.2 nm, 24.5 nm, and 22.4 nm for *n*-PentI, VA, and 5-AVAI, respectively. At the same time, the surface-treated samples display a finer surface texture and wider topographical features than the pristine, as evidenced by lower S_{pd} (peak density) and higher S_{al} (autocorrelation length). S_{pd} decreases from 8.3 μm^{-2} for the pristine surface to 3.61–5.7 μm^{-2} for the surface-treated surfaces. These features suggest smoother local surface textures with broader and more uniform grain formations in comparison to the pristine perovskite film. Additionally, the 5-AVAI-treated perovskite film shows significant differences in topographical descriptors to the other surfaces, in comparison to these parameters, with lower S_{dr} (2.2% compared to 4.0% of *n*-PentI and 5.7% of VA), lower S_{pd}, and longer S_{al}, indicating enhanced grain merging and smoother texturing. In contrast, VA- and *n*-PentI-treated films show a moderate increase in height variation, along with slight reductions in S_{pd} and modest increases in S_{al} from that of the pristine perovskite surface (see the full list of parameters and values in Table S2). These results align with the SEM images (Fig. 1e), supporting the conclusion that molecular passivation encourages grain growth and improves film uniformity. These changes highlight the need for a multi-dimensional roughness descriptor in surface analysis, as relying solely on average roughness values may overlook critical aspects of film morphology.

2.2. Optoelectronic characterization

The UV-vis absorption spectra of pristine and surface-treated perovskite films are shown in Fig. S4a, confirming

comparable light absorption characteristics across all the films. The treated perovskite layers exhibited absorption spectra nearly identical to that of the pristine film, with no intensity loss and a consistent absorption edge at 780 nm. Optical band gaps at 1.62 eV were closely matching for all the samples, estimated using the Tauc formula (Fig. S4b). In addition, the Urbach energy (E_U) of the perovskite films was also estimated by fitting the exponential region of the absorption edge, $\alpha = \alpha_o \exp(E/E_U)$, where α is the absorption coefficient, α_o is the material constant, and E is the photon energy (Fig. S4c).[36] The extracted values of 40 meV, 38 meV, 38 meV, and 39 meV were estimated for pristine, *n*-PentI, VA, and 5-AVAI samples, respectively, showing minimal variation in sub-bandgap disorder after the surface treatments.

To evaluate the impact of different functional groups on charge carrier recombination and extraction, we performed steady-state and transient photoluminescence (ssPL and trPL) and transient surface photovoltage (trSPV) measurements, on pristine and surface-treated perovskite films (*n*-PentI, VA, and 5-AVAI). When deposited without the HSL, perovskite films treated with *n*-PentI and 5-AVAI exhibited enhanced PL intensity compared to pristine films, whereas VA treatment resulted in PL

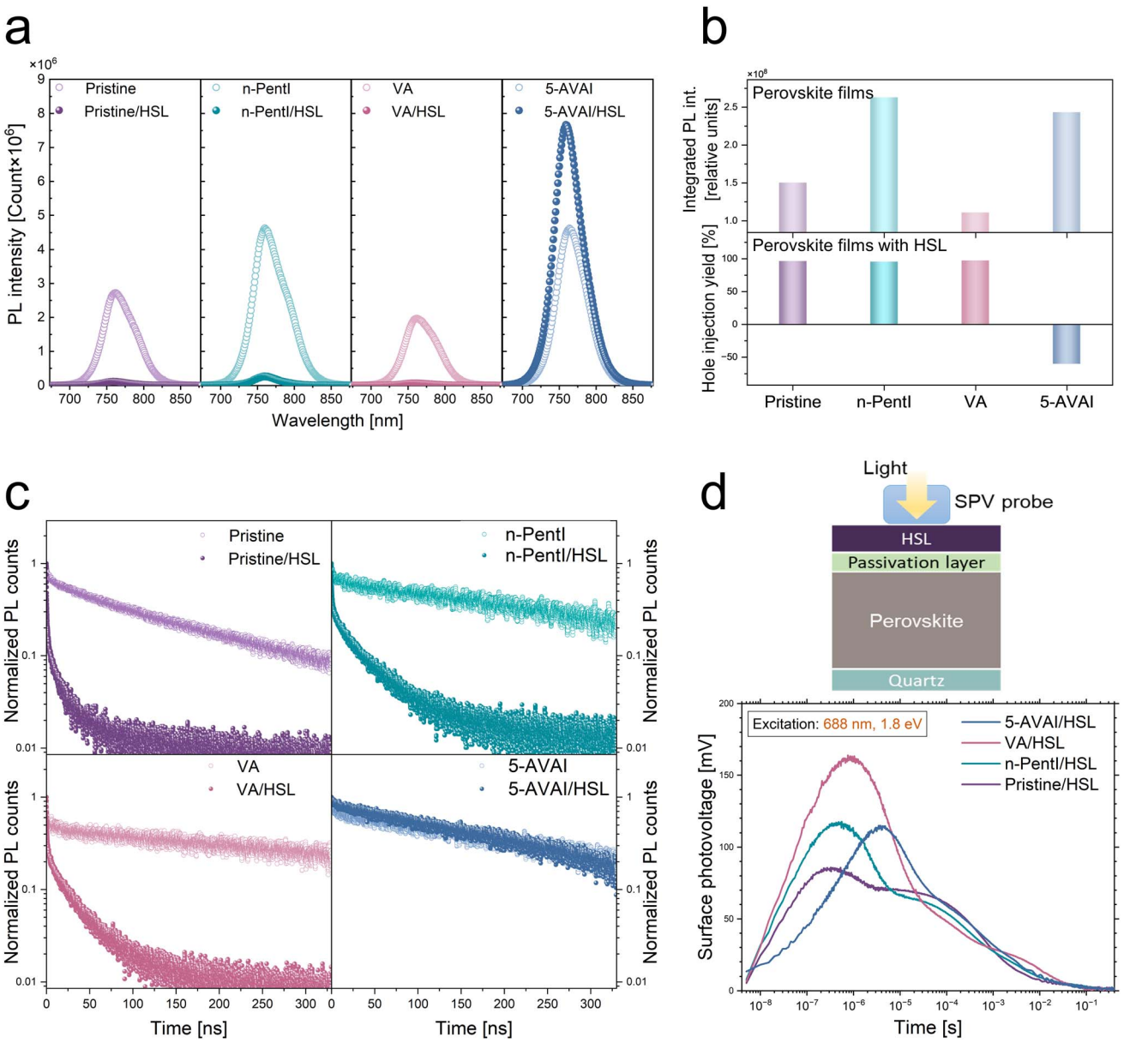

Fig. 3 Optoelectronic characterization. (a) Steady-state PL spectra of perovskite films and perovskite films with the HSL (spiro-OMeTAD). (b) Top: integrated PL intensity of the samples in panel (a), illustrating the relative PL intensity by integrating the area under the spectra; bottom: hole injection yield calculated from the percentage reduction in the PL intensity upon deposition of spiro-OMeTAD, indicating interfacial charge extraction efficiency. (c) trPL decay of perovskite fabricated on a glass substrate without and in the presence of an HSL. (d) Schematic illustration of the perovskite/passivation layer/HSL stack structure used for SPV measurements (top) and trSPV of perovskite films with the HSL measured at excitation sources of 688 nm (1.8 eV).

quenching (Fig. 3a and b upper panel). These results suggest that ammonium-containing molecules promote radiative recombination, while carboxylic acid groups reduce it. Notably, the PL intensity of the 5-AVAI-treated film was even higher when interfaced with the spiro-OMeTAD HSL, indicating reduced hole extraction efficiency. The percentage quenching of the PL intensity is given as hole injection yield (Fig. 3b lower panel) showing that the 5-AVAI layer between the perovskite and spiro-OMeTAD reduced the hole extraction into the HSL despite its surface passivation of the bottom perovskite layer.

To further examine the effect of surface treatments on recombination dynamics, we employed trPL measurements Fig. 3c. In the absence of an extraction layer, the pristine film exhibited the fastest PL decay among the samples, while all the molecule-treated films (*n*-PentI, VA, and 5-AVAI) showed slower decays (Fig. S5), indicating suppressed non-radiative recombination and improved carrier lifetime. Upon introduction of the HSL, the initial PL decay accelerated for the pristine and *n*-PentI-, and VA-treated films, consistent with efficient hole extraction. In contrast, the transient PL response of the 5-AVAI-treated film remained nearly unchanged compared to its HSL-free counterpart, corroborating the ssPL findings of limited hole extraction at the perovskite/spiro-OMeTAD interface. This may be ascribed to the alignment of the dipoles of the 5-AVAI molecules being perpendicular to the perovskite and spiro-OMeTAD layers.

Furthermore, differential lifetime analysis was applied to trPL data of the perovskite and perovskite/HSL samples, yielding comparable surface recombination velocity values for the samples treated with *n*-PentI and VA and the untreated pristine perovskite (Supporting Note 1 and Fig. S6).[37–39] The extracted surface recombination velocities align with their comparable hole injection yields shown in Fig. 3b, further confirming that *n*-PentI effectively passivates the surface traps of the perovskite layer while allowing efficient hole transfer into the HSL.

We apply trSPV under well-controlled conditions, to make a direct comparison between samples. In combination with C-AFM and PL, trSPV provides complementary insights into trap passivation and charge separation mechanisms. To directly measure the influence of the surface treatments on charge accumulation, extraction, and recombination dynamics at the perovskite/HSL interface, trSPV measurements were performed on half-cells (Fig. 3d) including pristine, *n*-PentI, VA, or 5-AVAI-treated perovskite.[40] The positive amplitude of the SPV transients reflects the extraction of photogenerated holes to the HSL surface, while electrons remain in the perovskite. The *n*-PentI-treated interface exhibits the highest maximum amplitude among the tested samples, indicating a higher density of extracted holes.[41] Additionally, hole extraction occurs most rapidly at the *n*-PentI-treated interface, as evidenced by the steepest initial slope within the first 100 ns after photoexcitation. In contrast, the delayed signal rise observed for the 5-AVAI-treated interface suggests impeded hole extraction, consistent with the trends observed in ssPL and trPL measurements. These trends are consistently observed across all excitation wavelengths (shown in Fig. S7b).

2.3. Solar cell performance of single junction devices

Encouraged by the role of the passivating molecules in modifying the interfacial properties and hole extraction ability, we investigated the effect of the functional groups on the photovoltaic performance by fabricating n–i–p structured PSCs in FTO/compact and mesoporous TiO_2/CsFAMA perovskite/passivation layer/spiro-OMeTAD/Au (FTO, fluorine-doped tin oxide; spiro-OMeTAD, 2,2′,7,7′-tetrakis[*N*,*N*-di(4-methoxyphenyl)amino]-9,9′-spirobifluorene; Au, gold) configuration. The schematic and a representative cross-section SEM image of the PSCs are shown in Fig. 4a and b, respectively.

The current density–voltage (*J*–*V*) characteristics of the best performing devices based on pristine and surface treated perovskite films, measured under 1-Sun illumination, are presented in Fig. 4c and the corresponding photovoltaic parameters are summarized in Table 1. Surface modification of the perovskite layer with *n*-PentI led to a substantial increase in the stabilized PCE. The champion PSC with the *n*-PentI surface-treated perovskite layer delivered the highest PCE of 20.7% among all the devices tested, including those with other surface passivators and the pristine control, accompanied by a V_{OC} of 1.13 V, J_{SC} of 23.14 mA cm^{-2}, and FF of 79%. In addition, the steady-state power outputs of the devices, which yielded stabilized PCE values consistent with those obtained from the *J*–*V* measurements, are shown in Fig. S8. The statistical box charts of the photovoltaic parameters (PCE, V_{OC}, J_{SC} and FF) for the four device categories are shown in Fig. 4d and the average photovoltaic performance parameters with standard deviations are listed in Table S3. The average V_{OC} of the devices with the passivation layers increased in comparison to the reference cells without the passivation layer, which is the result of the suppressed charge recombination process at the perovskite surface (Statistical significance among the four device categories is shown using Tukey's HSD post hoc analysis in Fig. S9). The increase in V_{OC} is in accordance with our previous findings from the trPL and trSPV measurements shown in Fig. 3.

Among the different passivation treatments, devices incorporating *n*-PentI exhibited the highest average V_{OC}, which correlates well with the strongest trSPV intensity observed in Fig. 3d. The enhanced trSPV signal suggests a significant reduction in charge recombination at the interface, leading to more efficient charge extraction and transport. *n*-PentI treatment effectively passivates the surface traps of the perovskite layer while still enabling efficient hole transfer into spiro-OMeTAD. Devices with VA and *n*-PentI treated perovskite show an improved FF compared to the pristine devices which can be ascribed to suppressed non-radiative recombination within the perovskite and its interface with the spiro-OMeTAD layer, the minimized carrier recombination, and improved charge extraction. The passivation effect of these molecules reduces defect states and optimizes charge transfer across the interface, thereby improving both V_{OC} and FF.

The trPL of the perovskite films showed the longer carrier lifetimes in the passivated perovskite films suggesting fewer non-radiative recombination pathways. The reduction of surface defects will lead to a higher density of photogenerated

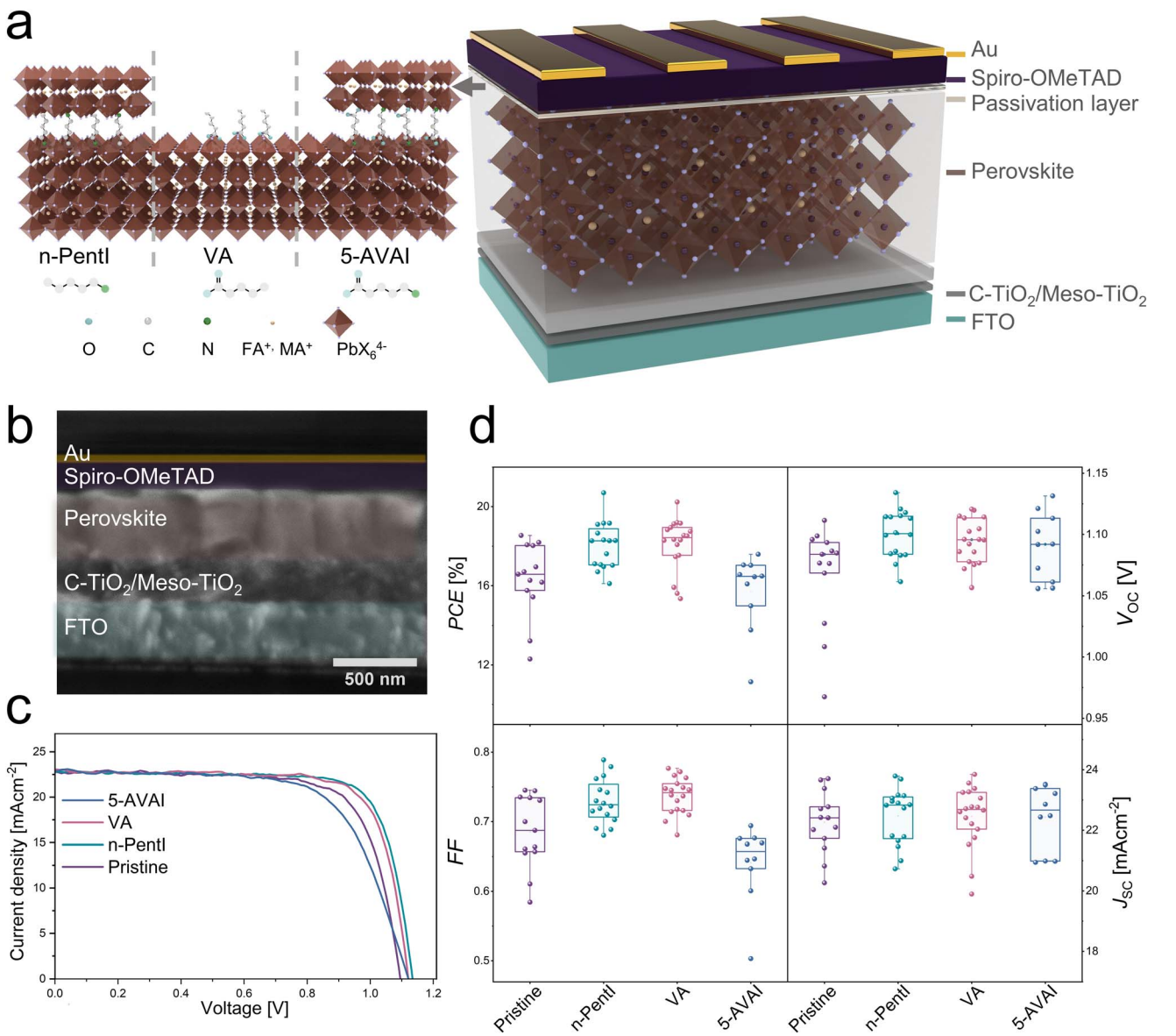

Fig. 4 Device architecture and performance. (a) Schematic of the device structure. (b) Cross-section SEM image of the device. (c) *J*–*V* curves (reverse scans) of the champion PSCs without and with passivation layers. (d) Statistical distributions of photovoltaic parameters of PSCs based on the pristine perovskite layer and perovskite layer passivated with *n*-PentI, VA, and 5-AVAI.

Table 1 The photovoltaic parameters of champion PSCs applying pristine and surface-treated perovskites

Perovskites	V_{OC} [V]	J_{SC} [mA cm^{-2}]	FF	PCE [%]
Pristine	1.10	22.71	0.74	18.55
n-PentI	1.13	23.14	0.79	20.70
VA	1.12	23.38	0.76	19.89
5-AVAI	1.12	22.85	0.68	17.28

charges under given illumination and therefore provide larger quasi-Fermi level splitting (QFLS) and V_{OC} values.[42] The QFLS/PL intensity trend shows a strong correlation in *n*-PentI-based devices, where the average V_{OC} is noticeably higher than that in pristine devices. However, PSCs based on the 5-AVAI-treated perovskite layer show a different trend. Although 5-AVAI yields similar PL enhancement to *n*-PentI, the corresponding V_{OC} improvement is only marginal. This discrepancy may be attributed to factors such as molecular orientation of the 5-AVAI layer on the surface, which could introduce an additional interfacial barrier and/or modify the band alignment at the interface. These effects may hinder efficient charge extraction into the HSL, as indicated by the significant drop in the FF in the corresponding devices and the absence of PL quenching when the HSL is deposited on top of the 5-AVAI layer, based on steady state PL measurements (Fig. 3a). Therefore, we hypothesized that while 5-AVAI provides surface passivation and thus PL enhancement similar to *n*-PentI, it might have also led to unfavorable interfacial charge extraction or band alignment between the perovskite and HSL. Fig. S10 shows the statistical

distribution of photovoltaic parameters from the forward scan direction.

A decreased series resistance was also observed in devices treated with *n*-PentI and VA surface passivators (Fig. S11), indicating improved charge carrier transport pathways that contributed to the overall enhancement in device performance. By contrast, disrupted hole transfer at the interface of the 5-AVAI surface-treated perovskite layer and spiro-OMeTAD led to a drop in the FF in the corresponding devices from 0.69 ± 0.05 to 0.64 ± 0.06 resulting in a reduced PCE in these devices compared to the pristine ones. This observed decline in the FF, which agrees well with the trPL and the lack of PL quenching in the HSL containing samples, unlike those with the other passivators (Fig. 3a), can be attributed to the insulating nature of the large spacer cation. The increased series resistance which disrupts efficient charge transport in 5-AVAI-containing devices is shown in Fig. S11. The negligible differences in J_{SC} of the samples show that J_{SC} is less sensitive to surface treatments than V_{OC} or the FF.

3. Conclusion

By employing organic passivating agents with identical alkyl backbones but distinct functional groups, this study investigates the impact of molecular functionality on interfacial morphology, the electronic structure, and the device performance of triple-cation perovskites. Combined structural and spectroscopic characterization studies reveal that surface passivation using molecules with single functional groups, such as carboxylic acid or ammonium, more effectively enhances device performance. The carboxylic acid group interacts with undercoordinated Pb^{2+} and metallic Pb^0 species at the surface, suppressing trap states. Ammonium-containing molecules induce favorable interfacial reconstruction to form 2D Ruddlesden–Popper phases, which mitigate non-radiative recombination. In particular, *n*-PentI treatment leads to the most pronounced improvements in charge extraction efficiency and photovoltage, as evidenced by trPL and trSPV measurements, ultimately boosting overall device performance. In contrast, 5-AVAI, while effective in defect passivation, forms an insulating interlayer that limits hole transport, highlighting the delicate balance between chemical passivation and charge extraction. VA treatment shows minimal structural modification but still contributes to improved performance. This work provides fundamental insights into structure–function relationships in interfacial molecular engineering. These insights offer guidance for rational design of molecular passivators while acknowledging that broader studies would be necessary to establish universal rules. By establishing a direct link between functional group identity, interfacial chemistry, and device operation, it offers a rational design framework for developing high-performance PSCs through tailored passivation strategies.

4. Experimental section

4.1. Perovskite film and interfacial layer fabrication

The perovskite precursor solution, composed of mixed cations (lead (Pb^+), cesium (Cs^+), formamidinium (FA^+), and methylammonium (MA^+)) and halides (I^- and Br^-) was dissolved in a mixed solvent (DMF/DMSO = 4 : 1) with the chemical formula of $Cs_{0.05}(FA_{0.83}MA_{0.17})_{0.95}Pb(I_{0.83}Br_{0.17})_3$. To prepare this solution, 1.5 M stock solutions of PbI_2 (TCI, >98% perovskite grade) and $PbBr_2$ (TCI, >98% perovskite grade) were prepared using 4 : 1 dimethylformamide, DMF (Sigma Aldrich, 99.8% anhydrous) and dimethyl sulfoxide, DMSO (Sigma Aldrich, 99.9% anhydrous). Formamidinium iodide (FAI, Greatcell Solar, >99.99%) and methylammonium bromide (MABr, Greatcell Solar, >99.99%) were then mixed with PbI_2 and $PbBr_2$, respectively, to form $FAPbI_3$ and $MAPbBr_3$.

The perovskite precursor solution was then prepared by mixing solutions of $FAPbI_3$ and $MAPbBr_3$ in a ratio to yield $(FAPbI_3)_{0.83}(MAPbBr_3)_{0.17}$ with an excess of PbI_2. 5% CsI (Abcr) was added to the mixture to form triple-cation perovskite $Cs_{0.05}(FA_{0.83}MA_{0.17})_{0.95}Pb(I_{0.83}Br_{0.17})_3$, CsFAMA, solution. Perovskite films were deposited by spin coating the precursor solution onto the substrates in a two-step spin coating starting at 1000 rpm and continuing with 6000 rpm for 20 s. 200 μl of chlorobenzene (CB, Sigma-Aldrich) was dropped onto the spinning sample during the last 5 s of the second step. The films were then annealed at 100 °C for 30–40 min. All steps were conducted under a nitrogen atmosphere inside a glovebox. For the surface passivation, the passivation molecules *n*-PentI (Greatcell solar), VA (Sigma Aldrich, >99%), and 5-AVAI (Greatcell solar) were dissolved in a 3 : 1 mixture of CB and IPA at a concentration of 10 mM. The interfacial layer was deposited on the annealed perovskite films by spin coating at 4000 rpm for 20 s, followed by annealing at 100 °C for 1 min.

4.2. Device fabrication

PSCs were fabricated based on the protocol described by Saliba *et al.*,[43] with minor modifications. The fluorine-doped tin oxide (FTO) substrates (TEC15, Greatcell Solar) were etched using a chemical etching process with zinc powder (Sigma-Aldrich) and 2 M HCl solution (Sigma-Aldrich). The FTO substrates were then cleaned sequentially in Hellmanex solution, deionized water, acetone, and IPA using sonication. After cleaning, the substrates were treated with a UV-ozone cleaner. The compact TiO_2 layer (c-TiO_2) was deposited *via* spray pyrolysis of a 0.16 M solution of titanium diisopropoxide bis(acetylacetonate) (Sigma-Aldrich) and 0.4 M acetylacetone (Sigma-Aldrich) in absolute ethanol (Altia, 99.5%) at 460 °C. The substrates were maintained at 460 °C on a hot plate and sprayed using an airbrush with compressed air.

A mesoporous TiO_2 layer was deposited on the compact layer by spin coating a 150 mg mL^{-1} suspension of TiO_2 nanoparticles (Greatcell Solar, 30 NR-D), followed by annealing at 450 °C for 30 min. The perovskite and interfacial layers were then deposited on the TiO_2-coated substrates under an inert atmosphere. Subsequently, a HSL of 70 mM spiro-OMeTAD (Lumtec), doped with 4-*tert*-butylpyridine (*t*BP, Sigma Aldrich), lithium bis(trifluoromethanesulfonyl)imide (LiTFSI, Sigma Aldrich), and tris(2-(1*H*-pyrazol-1-yl)-4-*tert*-butylpyridine)cobalt(III) tris(bis(trifluoromethanesulfonyl)imide) (FK209, Dyenamo), was deposited by spin coating at 4000 rpm for 20 s.

Finally, a gold electrode (80 nm) was thermally evaporated onto the samples.

4.3. Film characterization

XRD measurements were performed on a Bruker D8 Discover instrument (Karlsruhe, Germany). The pristine and treated perovskite films were scanned in a 2θ range of 2–45° at a fixed grazing incidence angle of 1° and a step size of 0.04°. The phase identification was done using the PDF-2 2020 database from ICDD. The XPS were collected using a Thermo Scientific Nexsa XPS system equipped with a monochromatized Al Kα X-ray source (1486.6 eV), a dual low-energy electron and a low-energy ion charge compensation system and a dual-mode MAGCIS ion source for sample cleaning and depth profiling.

The survey and the high-resolution spectra were measured using a pass energy of 200 eV and 50 eV, respectively. The possible X-ray damage was monitored by scanning so-called snapshot spectra of Pb 4f with 150 eV pass energy as the first and last step of the experiment for every sample. The base pressure of the analyzer chamber was on the 10^{-8} mbar level when the X-ray source and flood gun were turned off and about 3×10^{-7} mbar when scanning the spectra (Ar ion charge compensation increases the pressure). The probing depth of the XPS is in the range of 5–10 nm. The possible difference between the top surface layer perovskite and more bulk like perovskite was compared by carrying out gentle Ar cluster cleaning and depth profiling through the topmost few nanometers. The low energy Ar clusters were used to profile the surface by using clusters of 500 Ar ions with an energy of 6000 eV. The survey and the high-resolution spectra were recorded after every 20 s long etching cycle. The thickness of the removed layer was less than a few nanometers in total. The profiling (Ar cluster etching) was used to estimate the effect of air exposure and vacuum on the possible degradation of the surfaces. The spectra were fitted using the Igor Pro SPANCF fitting macro package.[44,45] The symmetric Voigt peak shape with a Lorentzian-to-Gaussian (L : G) ratio of 30 : 70 and Shirley background subtraction were used in the fitting. The binding energy calibration was done using the adventitious carbon C–C component at 284.8 eV as a reference.

Topographical analysis was carried out using a field emission SEM (FESEM, Apreo S, Thermo Scientific), operated at an accelerating voltage of 5 kV. Perovskite films were first deposited on glass substrates and subsequently mounted on aluminum stubs using copper tape and conductive carbon paste. Images were captured with a Trinity 1 detector, with a horizontal field width of 5 μm. For cross-section SEM of the PSCs, the imaging was carried out with an Everhart–Thornley detector and with a horizontal field width of 2.54 μm.

UV-Vis absorption measurements were carried out using a Shimadzu UV-3600 spectrophotometer, covering the UV to near-infrared range. ssPL spectra were obtained using an FLS1000 spectrofluorometer (Edinburgh Instruments, UK). trPL decay measurements were performed using a time-correlated single-photon counting (TCSPC) system. The setup included a PicoHarp 300 module for timing control and a PDL 800-B pulsed laser driver for excitation. A Hamamatsu R3809U-50 microchannel plate photomultiplier was used for detection, arranged in a 90° geometry.

trSPV measurements were carried out on a setup built in-house. All samples were encapsulated using thin cover glass and UV-curable glue (BluFixx MGS Transparent) to protect the sensitive perovskite films from air exposure. Laser excitation was incident on the spiro-OMeTAD exposed surface *via* a tunable pumped pulse laser (Nd:YAG Laser, EKSPLA, NT230-50-SH/SF-SCU-2H) at a pulse time of 3–6 ns, a frequency of 2 Hz, and photon energies from 1.4 eV to 3.0 eV. Laser fluence was controlled to be around 15.0 nJ cm^{-2} using neutral density filters. For each sample, 30 transients were recorded and averaged. The transients were measured with an oscilloscope card (Gage, CSE 1622-4GS, 200 MS s^{-1}) using custom-developed software for logarithmic readout.

The pristine and treated samples were imaged with Multimode 8 AFM in conductive AFM mode (Bruker, Billerica, MA). The cantilevers used were of the type SCM-PIT-V2 with a spring constant of $k = 3.0$ N m^{-1} and a nominal radius of curvature of $r = 25$ nm, as reported by the manufacturer (Bruker). Imaging was conducted at room temperature (23 ± 2 °C) and a relative humidity of 20 ± 3%. The images, of 5 μm × 5 μm size, were obtained at a resolution of 512 pixels × 512 pixels using the minimum force needed to maintain contact. Image analysis and processing were performed using MountainsSPIP v.9.3.10663 (DigitalSurf, Besançon, France). A range of roughness parameters were analysed. Briefly described, the amplitude parameters arithmetic average (S_a) and root-mean-square value (S_q) describe the height variation from the mean level of the image. These are calculated as either a S_a or a S_q. The autocorrelation length, S_{al}, provides a measure of 'lateral roughness' (compared to amplitude roughness S_a and S_q) and is defined as the distance over which the autocorrelation function decreases to 20% of its original value. Statistical distributions of heights are given by the descriptors skewness (S_{sk}), indicating the asymmetry of the distribution, and kurtosis (S_{ku}), describing the broadness of height distribution. For the kurtosis, a value of 3 corresponds to a normal Gaussian distribution (mesokurtic) and the developed surface area ratio (S_{dr}), which describes the percentage increase in surface area due to roughness compared to a perfectly flat surface. Finally, the point density, S_{pd}, was evaluated, giving a value of peaks per unit area (typically μm^2) that are surrounded by lower measurement points. S_{pd} is calculated after Wolf pruning.[46,47]

4.4. Device characterization

The current density–voltage (J–V) curves of PSCs were measured under ambient conditions under a solar simulator (Newport Oriel Instruments, model 92250A, 150 W xenon lamp) at an illumination intensity of 100 mW cm^{-2} (AM 1.5G) with a Keithley 2636 source measure unit. A mask with an aperture area of 11.5 mm^2 was used to define the active area of the devices for the measurements. The voltage scan was performed from −0.2 V to 1.2 V in a forward sweep and then from 1.2 V to −0.2 V in a reverse sweep with a scan rate of 10 mV s^{-1}. No preconditioning was carried out for the devices.

Author contributions

M. H.: conceptualization, investigation, methodology, formal analysis, visualization, and writing – original draft. T. W. G.: investigation, methodology, formal analysis, and writing – review and editing. G. K. G.: methodology and writing – review and editing. R. N.: visualization, formal analysis, and writing – review and editing. S. G. methodology, formal analysis, and writing – review and editing. P. V.: supporting and writing – review and editing. R. Ö.: supporting and writing – review and editing. J.-H. S.: conceptualization, methodology, funding acquisition and writing – review and editing. A. A.: conceptualization, methodology, and writing – review and editing. K. M.: conceptualization, supporting, funding acquisition, and writing – review and editing.

Conflicts of interest

There are no conflicts of interest to declare.

Data availability

The data supporting the findings of this study are available within the SI and openly available on Zenodo at [https://doi.org/10.5281/zenodo.15799811] under the Creative Commons Attribution 4.0 International License (CC BY 4.0).

Supplementary information is available. See DOI: https://doi.org/10.1039/d5el00156k.

Acknowledgements

M. H. thanks SUSMAT profiling funding (Research Council of Finland and the University of Turku). M. H. and R. N. thank the Research Council of Finland (project ECOSOL, 347275). K. M. thanks the Research Council of Finland for the BioEST project (346015 and 336577). P. V. thanks the Research Council of Finland, Decision No. 347772. This work is part of the Research Council of Finland Flagship Programme, Photonics Research and Innovation (PREIN), decision number 346511. The Strategic Materials Research Infrastructure (MARI) and Sustainable Fabrication (SusFab) infrastructure at the University of Turku were used for this study.

References

1 Best Research-Cell Efficiency Chart | Photovoltaic Research | NREL, https://www.nrel.gov/pv/cell-efficiency, accessed June 9, 2025.
2 Q. Dong, Y. Fang, Y. Shao, P. Mulligan, J. Qiu, L. Cao and J. Huang, *Science*, 2015, **347**, 967–970.
3 Y. Bai, Q. Dong, Y. Shao, Y. Deng, Q. Wang, L. Shen, D. Wang, W. Wei and J. Huang, *Nat. Commun.*, 2016, **7**, 12806.
4 C. M. Wolff, P. Caprioglio, M. Stolterfoht and D. Neher, *Adv. Mater.*, 2019, **31**, 1902762.
5 J. Tao, C. Zhao, Z. Wang, Y. Chen, L. Zang, G. Yang, Y. Bai and J. Chu, *Energy Environ. Sci.*, 2025, **18**, 509–544.
6 Z. Ni, C. Bao, Y. Liu, Q. Jiang, W.-Q. Wu, S. Chen, X. Dai, B. Chen, B. Hartweg, Z. Yu, Z. Holman and J. Huang, *Science*, 2020, **367**, 1352–1358.
7 C. Li, H. Li, Z. Zhu, N. Cui, Z. Tan and R. Yang, *Sol. RRL*, 2021, **5**, 2000579.
8 Y. Shao, Z. Xiao, C. Bi, Y. Yuan and J. Huang, *Nat. Commun.*, 2014, **5**, 5784.
9 L. Shen, P. Song, K. Jiang, L. Zheng, J. Qiu, F. Li, Y. Huang, J. Yang, C. Tian, A. K.-Y. Jen, L. Xie and Z. Wei, *Nat. Commun.*, 2024, **15**, 10908.
10 M. Hadadian, J.-P. Correa-Baena, E. K. Goharshadi, A. Ummadisingu, J.-Y. Seo, J. Luo, S. Gholipour, S. M. Zakeeruddin, M. Saliba, A. Abate, M. Grätzel and A. Hagfeldt, *Adv. Mater.*, 2016, **28**, 8681–8686.
11 Z. Yang, J. Dou, S. Kou, J. Dang, Y. Ji, G. Yang, W.-Q. Wu, D.-B. Kuang and M. Wang, *Adv. Funct. Mater.*, 2020, **30**, 1910710.
12 G. Wu, R. Liang, M. Ge, G. Sun, Y. Zhang and G. Xing, *Adv. Mater.*, 2022, **34**, 2105635.
13 K. A. Khawaja, S. N. Vijayaraghavan, S. Penukula, W. Xiang, N. Rolston, L. Li and F. Yan, *EES Sol.*, 2025, **1**, 620–631.
14 N. Ali, X. Wang and H. Wu, in *Modeling, Characterization, and Production of Nanomaterials*, ed. V. K. Tewary and Y. Zhang, Woodhead Publishing, 2nd edn, 2023, pp. 437–466.
15 K. Choi, J. Lee, H. I. Kim, C. W. Park, G.-W. Kim, H. Choi, S. Park, S. A. Park and T. Park, *Energy Environ. Sci.*, 2018, **11**, 3238–3247.
16 S. Y. Abate, Z. Yang, S. Jha, J. Emodogo, G. Ma, Z. Ouyang, S. Muhammad, N. Pradhan, X. Gu, D. Patton, D. Li, J. Cai and Q. Dai, *ACS Appl. Mater. Interfaces*, 2023, **15**, 25495–25505.
17 J. Zhuang, P. Mao, Y. Luan, X. Yi, Z. Tu, Y. Zhang, Y. Yi, Y. Wei, N. Chen, T. Lin, F. Wang, C. Li and J. Wang, *ACS Energy Lett.*, 2019, **4**, 2913–2921.
18 Y. Deng, X. Li and R. Wang, *Sol. Energy Mater. Sol. Cells*, 2021, **230**, 111242.
19 X. Zheng, B. Chen, J. Dai, Y. Fang, Y. Bai, Y. Lin, H. Wei, X. C. Zeng and J. Huang, *Nat. Energy*, 2017, **2**, 1–9.
20 E. A. Alharbi, A. Y. Alyamani, D. J. Kubicki, A. R. Uhl, B. J. Walder, A. Q. Alanazi, J. Luo, A. Burgos-Caminal, A. Albadri, H. Albrithen, M. H. Alotaibi, J.-E. Moser, S. M. Zakeeruddin, F. Giordano, L. Emsley and M. Grätzel, *Nat. Commun.*, 2019, **10**, 3008.
21 H. Song, J. Yang, S. G. Lim, J. Lee, W. H. Jeong, H. Choi, J. H. Lee, H. Y. Kim, B. R. Lee and H. Choi, *Chem. Eng. J.*, 2023, **454**, 140224.
22 S. Zhang, F. Ye, X. Wang, R. Chen, H. Zhang, L. Zhan, X. Jiang, Y. Li, X. Ji, S. Liu, M. Yu, F. Yu, Y. Zhang, R. Wu, Z. Liu, Z. Ning, D. Neher, L. Han, Y. Lin, H. Tian, W. Chen, M. Stolterfoht, L. Zhang, W. Zhu and Y. Wu, *Science*, 2023, **380**, 404–409.
23 Q. He, A. Chen, T. Zhang, X. Chen, X. Bian, G. Xu, S. Pan, T. Chen, J. Yu, Z. Zhang, H. Zhu, G. Lu, O. M. Bakr and J. Pan, *Cell Rep. Phys. Sci.*, 2024, **5**, 102030.
24 S. Mathew, N. Nishimura, A. Kogo, T. Itoh, K. Yamamoto, Y. Hinuma and T. N. Murakami, *ACS Appl. Energy Mater.*, 2025, **8**, 4962–4972.

25 C. Stecker, K. Liu, J. Hieulle, R. Ohmann, Z. Liu, L. K. Ono, G. Wang and Y. Qi, *ACS Nano*, 2019, **13**, 12127–12136.
26 L. Fu, H. Li, L. Wang, R. Yin, B. Li and L. Yin, *Energy Environ. Sci.*, 2020, **13**, 4017–4056.
27 Z. Guo, M. Yuan, G. Chen, F. Liu, R. Lu and W.-J. Yin, *Advanced Science*, 2024, **11**, 2305799.
28 C. A. R. Perini, A.-F. Castro-Mendez, T. Kodalle, M. Ravello, J. Hidalgo, M. Gomez-Dominguez, R. Li, M. Taddei, R. Giridharagopal, J. Pothoof, C. M. Sutter-Fella, D. S. Ginger and J.-P. Correa-Baena, *ACS Energy Lett.*, 2023, **8**, 1408–1415.
29 C. Xu, L. Zuo, P. Hang, X. Guo, Y. Pan, G. Zhou, T. Chen, B. Niu, X. Xu, Z. Hong, D. Wang, H. Zhu, X. Yu, D. Yang and H. Chen, *J. Mater. Chem. A*, 2022, **10**, 9971–9980.
30 J. Wang, J. Zhang, Y. Zhou, H. Liu, Q. Xue, X. Li, C.-C. Chueh, H.-L. Yip, Z. Zhu and A. K. Y. Jen, *Nat. Commun.*, 2020, **11**, 177.
31 M. Saliba, T. Matsui, J.-Y. Seo, K. Domanski, J.-P. Correa-Baena, M. K. Nazeeruddin, S. M. Zakeeruddin, W. Tress, A. Abate, A. Hagfeldt and M. Grätzel, *Energy Environ. Sci.*, 2016, **9**, 1989–1997.
32 S. Wang, F. Cao, Y. Wu, X. Zhang, J. Zou, Z. Lan, W. Sun, J. Wu and P. Gao, *Mater. Today Phys.*, 2021, **21**, 100543.
33 Y. Hu, L. M. Spies, D. Alonso-Álvarez, P. Mocherla, H. Jones, J. Hanisch, T. Bein, P. R. F. Barnes and P. Docampo, *J. Mater. Chem. A*, 2018, **6**, 22215–22225.
34 N. Wei, Y. Chen, Y. Miao, T. Zhang, X. Wang, H. Wei and Y. Zhao, *J. Phys. Chem. Lett.*, 2020, **11**, 8170–8176.
35 C. Zhang, A. Baktash, J. A. Steele, D. He, S. Ding, S. Penukula, M. Hao, R. Lin, J. Hou, N. Rolston, M. Lyu, P. Chen, W.-Q. Wu and L. Wang, *Adv. Funct. Mater.*, 2024, **34**, 2315897.
36 E. Ugur, M. Ledinský, T. G. Allen, J. Holovský, A. Vlk and S. De Wolf, *J. Phys. Chem. Lett.*, 2022, **13**, 7702–7711.
37 T. Kirchartz, J. A. Márquez, M. Stolterfoht and T. Unold, *Adv. Energy Mater.*, 2020, **10**, 1904134.
38 L. Krückemeier, B. Krogmeier, Z. Liu, U. Rau and T. Kirchartz, *Adv. Energy Mater.*, 2021, **11**, 2003489.
39 M. Liu, S. Dahlström, C. Ahläng, S. Wilken, A. Degterev, A. Matuhina, M. Hadadian, M. Markkanen, K. Aitola, A. Kamppinen, J. Deska, O. Mangs, M. Nyman, P. D. Lund, J.-H. Smått, R. Österbacka and P. Vivo, *J. Mater. Chem. A*, 2022, **10**, 11721–11731.
40 F. Scheler, S. Mariotti, D. Mantione, S. Shah, D. Menzel, H. Köbler, M. Simmonds, T. W. Gries, J. Kurpiers, V. Škorjanc, J. Li, A. Al-Ashouri, P. Wagner, S. P. Harvey, F. Yang, M. Rusu, T. Unold, B. Stannowski, K. Zhu, F. Lang, D. Neher, E. Unger, A. Abate, D. Mecerreyes, M. Stolterfoht, E. Köhnen, L. Korte, M. Topič and S. Albrecht, *Adv. Energy Mater.*, 2025, **15**(16), 2404726.
41 Z. Iqbal, T. W. Gries, A. Musiienko and A. Abate, *Sol. RRL*, 2024, **8**, 2400329.
42 S. Yang, J. Dai, Z. Yu, Y. Shao, Y. Zhou, X. Xiao, X. C. Zeng and J. Huang, *J. Am. Chem. Soc.*, 2019, **141**, 5781–5787.
43 M. Saliba, J.-P. Correa-Baena, C. M. Wolff, M. Stolterfoht, N. Phung, S. Albrecht, D. Neher and A. Abate, *Chem. Mater.*, 2018, **30**, 4193–4201.
44 E. Kukk, G. Snell, J. D. Bozek, W.-T. Cheng and N. Berrah, *Phys. Rev. A*, 2001, **63**, 6062702.
45 H. Lee, B. G. Whetten, B. Jae Kim, J. Young Woo, Y. Koo, J. Bae, M. Kang, T. Moon and H. Joo, *Phys. Rev. Lett.*, 2024, **132**(16), 133001.
46 R. Deltombe, K. J. Kubiak and M. Bigerelle, *Scanning*, 2014, **36**, 150–160.
47 D. Whitehouse, in *Surfaces and Their Measurement*, ed. D. Whitehouse, Kogan Page Science, Oxford, 2002, pp. 48–95.